Two years of satellite-based carbon dioxide emission quantification at the world's largest coal-fired power plants

Daniel H. Cusworth[1,2], Andrew K. Thorpe[3], Charles E. Miller[3], Alana K. Ayasse[1], Ralph Jiorle[1], Riley M. Duren[1,2,3], Ray Nassar[4], Jon-Paul Mastrogiacomo[5], and Robert R. Nelson[3]

[1]Carbon Mapper, Pasadena, CA, USA
[2]Arizona Institutes for Resilience, University of Arizona, Tucson, AZ, USA
[3]Jet Propulsion Laboratory, California Institute of Technology, Pasadena, CA, USA
[4]Environment & Climate Change Canada, Toronto, ON, Canada
[5]University of Toronto, Toronto, ON, Canada

Corresponding Author: Daniel H. Cusworth (dan@carbonmapper.org)

Abstract

Carbon dioxide (CO_2) emissions from combustion sources are uncertain in many places across the globe. Satellites have the ability to detect and quantify emissions from large CO_2 point sources, including coal-fired power plants. In this study, we made observations with the PRecursore IperSpettrale della Missione Applicativa (PRISMA) satellite imaging spectrometer and the Orbiting Carbon Observatory-3 (OCO-3) instrument onboard the International Space Station at over 30 coal-fired power plants routinely between 2021-2022. CO_2 plumes were detected in 50% of acquired PRISMA scenes, which is consistent with the combined influence of viewing parameters on detection (solar illumination, surface reflectance) and unknown factors (like daily operational status). We compare satellite-derived emission rates to *in situ* stack emission observations and find average agreement to within 27% for PRISMA and 30% for OCO-3, though more observations are needed to robustly characterize the error. We highlight two examples of fusing PRISMA with OCO-2 and OCO-3 observations in South Africa and India. For India, we acquired PRISMA and OCO-3

observations on the same day and use the high spatial resolution capability of PRISMA (30 m spatial/pixel resolution) to partition relative contributions of two distinct emitting power plants to the net emission. Though an encouraging start, two years of observations from these satellites did not produce sufficient observations to estimate annual average emission rates within low (<15%) uncertainties. However, as the constellation of CO_2-observing satellites is poised to significantly improve in the coming decade, this study offers an approach to leverage multiple observation platforms to better quantify and characterize uncertainty for large anthropogenic emission sources.

1 Introduction

Anthropogenic carbon dioxide (CO_2) emissions are dominated by strong discrete point sources: power and other industrial combustion are estimated to make up 59% of global anthropogenic CO_2 emissions with transport, buildings, and other sources making up the remaining 20%, 9%, and 12%, respectively (Crippa et al., 2022). Fossil fuel combustion is the largest contributor to warming trends globally since the pre-industrial era (IPCC, 2021). However, there remains uncertainty in the total magnitude of emissions from these sectors as bottom-up emission estimates rely on reported emission factors and activity data, which may vary in granularity and quality across countries and provinces (Hong et al., 2017; Guan et al., 2017). Accurate CO_2 emission quantification is important in light of the Paris Agreement, as participating countries must develop plans and report progress to reduce their country’s greenhouse gas (GHG) emissions (UN, 2015). Leveraging atmospheric measurements, particularly satellite remote sensing, can help reduce uncertainty in facility-level CO_2 emission estimates, provided that the observations are accurate and sufficiently sample the facility in time (Hill and Nassar, 2019). Deployed systematically with robust error characterization, this system could be an anchor towards assessing and verifying anticipated

CO_2 emission reductions as part of national and global GHG emission reduction plans and agreements.

Several studies have shown that atmospheric sounding satellites can accurately quantify some point source CO_2 emissions from large individual coal-fired power plants. First, the Orbiting Carbon Observatory-2 (OCO-2; Crisp et al., 2017) is a space-based instrument that observes solar backscattered near-infrared radiance in the oxygen *A* band (758-772 nm; 0.04 nm spectral resolution), the weak CO2 band (1594-1619 nm; 0.08 nm spectral resolution), and strong CO2 band (2042-2082 nm; 0.10 nm spectral resolution). OCO-2 views in nadir mode over land, while sun glint mode increases the signal over water giving measurements both land and water, and target mode to target specific validation or calibration sites. With its 10-km wide swath, $\leq$1.3x2.25 km^2 pixel resolution, and better than 1.0 ppm precision for retrievals of the column-mean dry-air mole fraction of CO_2 (XCO_2) (Taylor et al., 2023), OCO-2 is sensitive to single CO_2 point sources that emit sufficiently close to an OCO-2 orbital track and are spatially isolated from other major CO_2 sources. Using satellite observations from OCO-2, Nassar et al. (2017) detected strong CO_2 enhancements in the near vicinity of seven large coal-fired power plants and employed a Gaussian plume model emission quantification technique to estimate emission rates for these facilities. Further study expanded the set of facilities that could be quantified by OCO-2 (Nassar et al., 2021). Other studies have leveraged the nitrogen dioxide (NO_2) retrieval capability and wide swath of the TROPOspheric Monitoring Instrument (TROPOMI; van Geffen et al., 2020) to attribute and corroborate strong CO_2 signals seen in OCO-2 observations (Hakkarainen et al., 2021; Reuter et al., 2019). The Orbiting Carbon Observatory-3 (OCO-3; Eldering et al., 2019), the flight spare of OCO-2, has been on board the International Space Station (ISS) since May 2019. Like OCO-2, it has been shown capable of quantifying CO_2 power plant emissions. Nassar et al. (2022) analyzed nine successful OCO-3 acquisitions of the Bełchatów Power Station and found the variability in satellite-based emission estimates agreed well with the variability in independently reported hourly power generation. Guo et al., (2023) estimated emissions at Chinese power plants using OCO-2/3 and found close agreement with emission inventories. OCO-3 is different than OCO-2 in that it has a two-axis Pointing Mirror Assembly (PMA) for more agile pointing, allowing it to rapidly point off-nadir and take Snapshot Area Mapping (SAM) mode observations over the course of two minutes. These SAMs are approximately 80×80 km^2 collections of measurements and are typically over sites of interest including cities, power plants, volcanoes, and flux towers.

Another class of remote sensing imaging spectrometers – sometimes also referred to as hyperspectral imagers – also have been shown capable of detecting and quantifying strong CO_2 signals from large point sources. Thorpe et al. (2017) flew the Next-Generation Airborne/Infrared Imaging Spectrometer (AVIRIS-NG) over a coal-fired power plant in Four Corners, New Mexico, and detected strong CO_2 plumes. AVIRIS-NG observes a large range of solar backscattered radiance (380-2500 nm), but at much coarser spectral resolution (5 nm), and high spatial resolution (e.g., 3 m when flown at 3 km altitude). The much finer spatial resolution of AVIRIS-NG allows for improved visualization of the origin of a CO_2 plume, but at the expense of fine precision for a single observed CO_2 column. Still, Cusworth et al. (2021) analyzed a combination of AVIRIS-NG and the identically built Global Airborne Observatory (GAO) at over 20 power plants in the U.S., quantified emission rates, and found close agreement with continuous emissions monitoring (CEMS) hourly emission observations. From space, the PRecursore IperSpettrale della Missione Applicativa (PRISMA), launched in 2019, like AVIRIS-NG and GAO is sensitive to a large range of solar backscattered radiance (400-2500 nm), albeit at coarser spectral and spatial resolution (10 nm spectral resolution; 30 m spatial resolution; Loizzo et al., 2018). PRISMA is a tasked satellite instrument potentially capable of hundreds of 30×30 km^2 observations per day, with equatorial crossing time of 10:30am, and target revisit of seven days, though true revisit depends on tasking priorities of the system. Cusworth et al. (2021) showed a few examples of CO_2 plumes detected and quantified with PRISMA, with quantified emissions similar in magnitude to reported CEMS emissions..

The capacity for satellites to be leveraged as useful tools for reducing uncertainty in the global CO_2 anthropogenic emission sector requires synthesis and routine observations (i.e., tasking) of a critical number of facilities. Therefore, in this study, we made observations at a subset of global coal-fired power plants routinely over the course of two years to probe detection limits, emission quantification uncertainty, and data yields. We observed these facilities with both OCO-3 and PRISMA. To our knowledge to date, this study represents the largest satellite-based facility scale investigation of direct CO_2 emission quantification across a diverse set of global power plants, and the first investigation to assess the capability of PRISMA to reliably detect and quantify CO_2 point sources. The results, though not sufficient by themselves to reduce uncertainty relative to bottom-up inventories significantly on an annual basis, show a path forward for data fusion and synthesis of observations from the growing constellation of planned CO_2 sensing satellites.

2 Methods

Table 1 lists the locations of all power plants we targeted during this study between 2021-2022 with PRISMA. OCO-3 includes a subset of these sites as well as other fossil fuel combustion sites as part of its list of possible targets. We identified coal-fired power plants to routinely target using a combination of bottom-up and top-down information. Bottom-up coal-fired power plant CO_2 emission estimates rely on activity data, that usually includes permitted capacity of a power plant and its operational state; and emission factors, usually estimated from the composition of the coal that is combusted. Inventories, like the Global Energy Monitor (GEM), include this data for a large set of coal-fired power plants across the globe (GEM, 2023). From the GEM database, we gathered the top 10 largest bottom-up coal-fired power plants globally. We then gathered a list of top-down TROPOMI NO_2 combustion hotspots, as inferred by Beirle et al. (2021). We included an additional seven unique power plants using this dataset. Because the imaging scene size of PRISMA is 30 × 30 km^2, some adjacent smaller power plants were imaged simultaneously along with these larger power plants. In total, outside of the U.S., we made PRISMA observations at 27 power plants. In the U.S., we chose 10 power plants to routinely target using reported EPA CEMS information (campd.epa.gov): five of the top 30 emitting power plants, and five progressively lower emitters, chosen so that we could assess satellite detection capabilities.

Table 1. Power plants that were targeted specifically by PRISMA in this study.

Power Plant Name	**Country**	**Latitude**	**Longitude**	**Number clear-sky observations**	**Number plume detections**	**Minimum quantified CO2 emission (kt CO2 h^{-1})**	**Mean quantified CO2 emission (kt CO2 h^{-1})**	**Maximum quantified CO2 emission (kt CO2 h^{-1})**
Mundra-Adani	India	22.82	69.55	12	7	0.49±0.07	1.09±0.19	1.76±0.32
Korba-Balco	India	22.40	82.74	5	1	NA*	NA	NA
PLN Paiton Baru	Indonesia	-7.71	113.57	4	2	NA	NA	NA
Craig	USA	40.46	-107.59	5	5	0.56±0.11	0.69±0.16	0.8±0.22
Cumberland	USA	36.39	-87.65	1	0	NA	NA	NA
Dry Fork	USA	44.39	-105.46	6	3	0.61±0.09	0.65±0.13	0.69±0.16
H L Spurlock	USA	38.70	-83.82	5	3	1.15±0.32	1.26±0.39	1.37±0.45
Ulsan Hanju (1)	South Korea	35.49	129.33	1	0	NA	NA	NA
Hasdeo	India	22.41	82.69	5	0	NA	NA	NA
Hekinan	Japan	34.83	136.96	6	4	0.72±0.47	3.88±1.09	8.35±2.14
Baotou-1	China	40.66	109.66	5	2	0.19±0.07	0.27±0.07	0.35±0.07
Kendal	South Africa	-26.09	28.97	7	2	0.85±0.13	0.85±0.13	0.85±0.13
NTPC Korba	India	22.39	82.68	6	1	1.28±0.27	1.28±0.27	1.28±0.27

Kriel	South Africa	-26.25	29.18	8	3	0.74±0.15	0.82±0.15	0.95±0.16
Labadie	USA	38.56	-90.84	4	4	0.73±0.18	0.73±0.18	0.73±0.18
Martin Lake	USA	32.26	-94.57	8	8	1.45±0.31	2±0.59	2.6±0.98
Matimba	South Africa	-23.67	27.61	11	8	0.33±0.05	0.72±0.16	1.14±0.32
Matla	South Africa	-26.28	29.14	8	3	0.33±0.05	0.77±0.15	1.37±0.27
Medupi	South Africa	-23.71	27.56	15	12	0.33±0.06	0.83±0.19	1.47±0.34
Mundra-Tata	India	22.82	69.53	12	5	0.38±0.09	0.74±0.13	1.32±0.21
Niederaussem	Germany	51.00	6.67	1	0	NA	NA	NA
Oregon	USA	41.67	-83.44	5	1	NA	NA	NA
Paiton-3	Indonesia	-7.71	113.58	4	4	1.54±0.37	3.16±0.69	4.78±1.02
Rihand	India	24.03	82.79	8	5	0.83±0.17	0.99±0.26	1.36±0.38
Sanfeng	China	40.66	109.76	6	0	NA	NA	NA
Sasan	India	23.98	82.63	9	7	0.65±0.15	1.01±0.24	1.51±0.31
Sooner	USA	36.45	-97.05	6	3	1.05±0.22	1.05±0.22	1.05±0.22
Togtoh	China	40.20	111.36	2	2	0.25±0.06	0.91±0.17	1.58±0.27
Ulsan Hanju (2)	South Korea	35.47	129.38	1	0	NA	NA	NA
Vindhyachal	India	24.10	82.68	9	7	0.33±0.1	0.72±0.15	1.24±0.23
Waigaoqiao	China	31.36	121.60	6	1	NA	NA	NA
Yeosu Hanwha	South Korea	34.84	127.69	2	0	NA	NA	NA
Yosu	South Korea	34.83	127.67	2	0	NA	NA	NA
Al Zour	Kuwait	28.71	48.37	12	0	NA	NA	NA

*A value of “NA” indicates that no plumes were detected at this power plant or that the emission quantification algorithm (described in Methods) failed to quantify an emission rate.

2.1 PRISMA observations and quantification

PRISMA is a tasked satellite instrument, capable of collecting around 200 30 × 30 km^2 targets per day and has 20° pointing capability off nadir. Authenticated users can program single observation requests through PRISMA’s web portal (prisma.asi.it), which currently allows for 13 concurrent requests at a time per user. We specified two-week observing windows for each request, and configured requests to collect if the scene-averaged solar zenith angle (SZA) was less than 70° and forecast meteorology anticipated less than 20% cloud cover. If the orbital configuration, weather, SZA align and there are no other conflicting or higher priority requests, PRISMA images a target.

For each acquired PRISMA image, we performed XCO_2 retrievals on all pixels within a 2.5 km radius around the power plant. We retrieve XCO_2 using the Iterative Maximum A Posteriori – Differential Optical Absorption Spectroscopy (IMAP-DOAS) algorithm, as implemented in Cusworth et al. (2021). This approach estimates XCO_2 by decomposing an observed radiance spectrum into high and low frequency features between 1900-2100 nm. For high-frequency features, we simulate atmospheric transmission of CO_2, H_2O, and N_2O using a Beer-Lambert approximation. For low-frequency features (e.g., surface reflectance, aerosol scattering), we use an 8-degree polynomial. The forward model that drives IMAP-DOAS therefore has the following form:

$$F^h(\mathbf{x}) = I_0(\lambda) \exp\left(-\sum_{n=1}^{6} s_n \sum_{l=1}^{72} A_l \tau_{n,l}\right) \sum_{k=0}^{K} a_k \lambda^k \quad (1)$$

Where F^h is simulated backscattered radiance at wavelength λ, I_0 is incident solar intensity, A_l is the airmass factor at vertical level $l \in [1,72]$, $\tau_{n,l}$ is the optical depth for each trace gas element, s_n is the scaling factor applied to the optical depth, and a_k is a polynomial coefficient (K=8). Optical depths are computed by querying meteorological information for pressure and temperature from the MERRA-2 reanalysis (Gelaro et al., 2017), and using that information to select proper HITRAN absorption cross sections for each trace gas (Kochanov et al., 2016). To compare the model from Equation 1 against PRISMA observed radiance ($\mathbf{y}$), we compute $F^h(\mathbf{x})$ between 1900-2100 nm at 0.02 nm resolution, then convolve the output using the PRISMA full-width half maximum, and sample at PRISMA wavelength positions. This results in vector $\mathbf{F}(\mathbf{x})$ that is comparable to $\mathbf{y}$. The vector $\mathbf{x}$, also called the state vector, includes scale factors for CO_2, H_2O, N_2O, and polynomial coefficients: $\mathbf{x} = (s_{CO2}, s_{H2O}, s_{N2O}, a_o, \dots, a_8)$.

XCO_2 is retrieved from PRISMA radiance using a Bayesian optimal estimation approach (Rodgers, 2000). Here, the optimized state vector solution, or posterior, is solved through Gauss-Newton iteration:

$$\mathbf{x}_{i+1} = \mathbf{x}_{\mathbf{A}} + (\mathbf{K}_i^{\boldsymbol{T}} \mathbf{S}_{\mathbf{O}}^{-\mathbf{1}} \mathbf{K}_i + \mathbf{S}_{\mathbf{A}}^{-\mathbf{1}})^{-1} \mathbf{K}_i^{\boldsymbol{T}} \mathbf{S}_{\mathbf{O}}^{-\mathbf{1}} [y - \mathbf{F}(\mathbf{x}_i) + \mathbf{K}_{\boldsymbol{i}}(\mathbf{x}_{\boldsymbol{i}} - \mathbf{x}_{\mathbf{A}})] \quad (2)$$

Where $\mathbf{S}_O = [\boldsymbol{\varepsilon\varepsilon}^T]$ is the observation error covariance matrix defined by the instrument signal to noise ratio (SNR), $\mathbf{x}_A$ is the prior estimate of the state vector, and $\mathbf{S}_A$ is the prior error covariance matrix. The matrix $\mathbf{K}$, or Jacobian matrix, represents the first derivative of the $\mathbf{F}(\mathbf{x})$ with respect to the state vector:

$$\mathbf{K}_i = \left.\frac{\partial \mathbf{F}}{\partial \mathbf{x}}\right|_{\mathbf{x}=\mathbf{x}_i} \quad (3)$$

The posterior error covariance matrix can be computed explicitly to quantify retrieval precision:

$$\hat{\mathbf{S}} = \left(\mathbf{K}_i{}^T \mathbf{S}_{\mathrm{O}}^{-1} \mathbf{K}_i + \mathbf{S}_{\mathrm{A}}^{-1}\right)^{-1} \quad (4)$$

Across the scenes we acquired with PRISMA, using this retrieval approach, we quantify an average 3.3 ppm precision for an XCO_2 column. Absolute biases in PRISMA XCO_2 retrievals are less important for CO_2 plume detection and quantification: systematic retrieval biases are removed from a scene through the quantification and removal of a local background, as described below. To characterize bias in emission quantification, we compare emission rates derived from PRISMA to stack-level CEMS measurements (Section 3.2).

We quantified emissions for each PRISMA plume detection using the Integrated Mass Enhancement (IME) approach (Cusworth et al., 2021). However, we updated the masking scheme for this analysis to produce more reliable masks for each CO_2 plume. Figure 1 shows the plume masking procedure for a plume detected at the Hekinan, Japan power plant on July 19, 2021. First, we apply a background threshold to differentiate candidate plume pixels from the background (method to quantify background threshold described in Section 3.2). We then group enhanced XCO_2 pixels into clusters of at least 20 connected pixels. These groups are then buffered with a one-pixel dilation filter to smooth edges and any gaps that exist in a group (Dougherty, 1992). Finally, each cluster is considered part of the plume if at least one of its pixels is within 500 m of an exhaust stack.

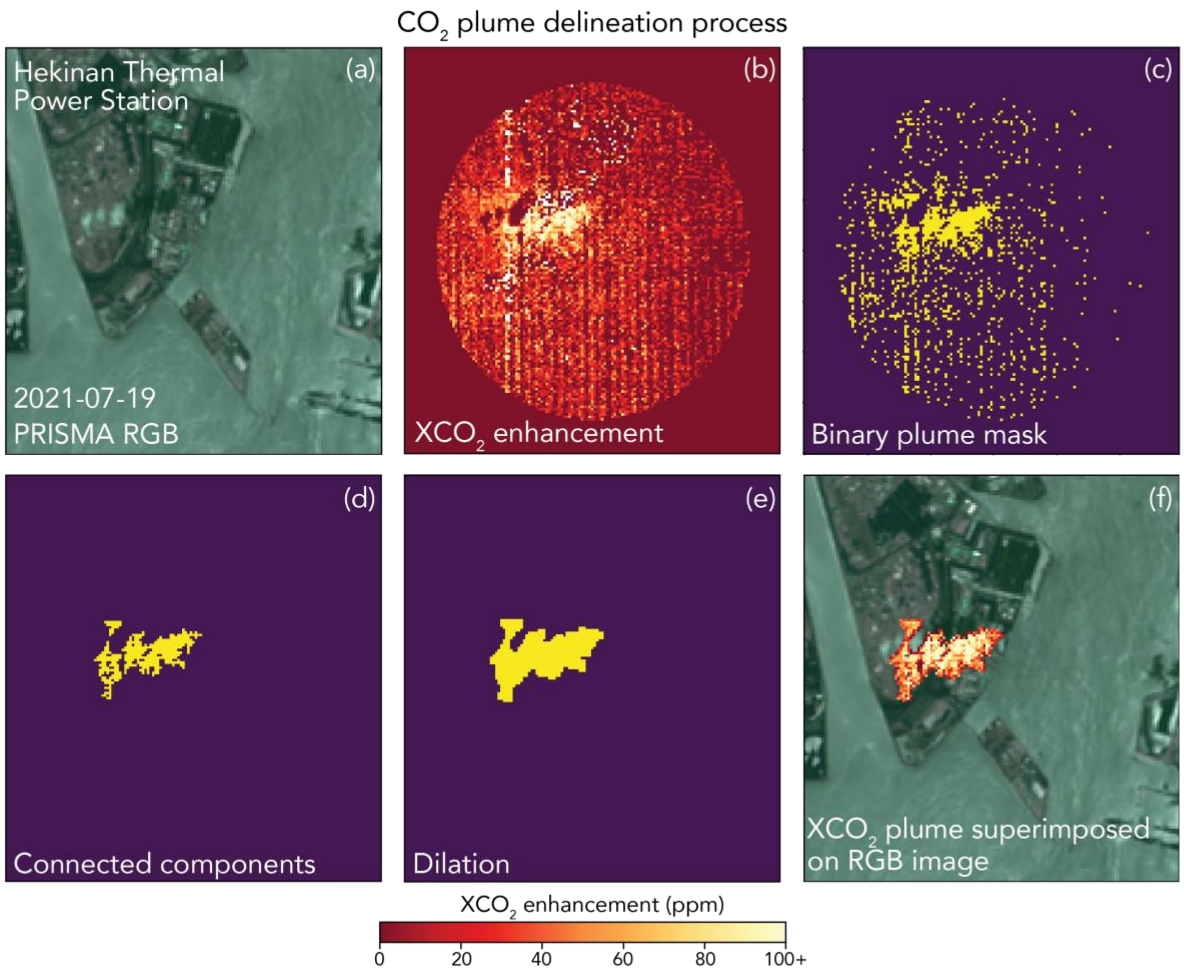

Figure 1. Example of the plume delineation and masking process performed on XCO_2 retrievals derived from PRISMA observations. Panel (a) shows the simultaneously observed RGB PRISMA imagery, panel (b) shows retrieved XCO_2 above the background, panels (c)-(e) show the plume masking procedure to isolate enhanced pixels and remove noise, and panel (f) shows the resulting CO_2 plume superimposed on the RGB imagery.

IME is calculated for a plume using the following equation:

$$\mathrm{IME} = \sum_{i=1}^{N} \Delta\Omega_i \, \Lambda_i \quad (5)$$

where $\Delta\Omega_i$ is the XCO_2 mass enhancement in pixel i relative to background (kg m^{-2}), Λ_i is the pixel area (900 m^2), and N is the number of pixels in the plume. The CO_2 emission rate Q is estimated from the IME using the following relationship:

$$Q = \frac{U_{eff}}{L} \, \mathrm{IME} \quad (6)$$

where $L = \sqrt{\sum_{i=1}^{N} \Lambda_i}$ is the plume length and U_{eff} is the effective wind speed. The parameter L is an operational parameter that needs to be related to the extent of the plume. Since a plume dissipates in all directions due to turbulent diffusion, an explicit scaling function (i.e., an effective wind speed U_{eff}) that relates L and 10 m wind speed (U_{10}) to the true emission can be derived through large eddy simulations (Varon et al., 2018):

$$U_{eff} = 1.1 \log U_{10} + 0.6. \quad (7)$$

where U_{eff} and U_{10} are in units of [m s^{-1}]. We query the ERA5-Land reanalysis using the Open-Meteo Application Programming Interface (open-meteo.com), which provides hourly wind information globally at 0.1° spatial resolution (Muñoz-Sabater et al., 2021). Uncertainty due to winds is calculated by generating an ensemble of U_{10} values assuming 50% error (Cusworth et al., 2021). Uncertainty due to the CO_2 background is calculated by generating many emission estimates and calculating a standard deviation using an ensemble of background thresholds. Background thresholds are set to vary with scene-averaged CO_2 retrieval precision. Total emission uncertainty is estimated by adding in quadrature the contribution of wind and background uncertainties.

2.2 OCO-3 observations and quantification

OCO-3 is also a tasked mission: it can take SAMs over any place of interest within the latitude range of the ISS orbit (about 52° S to 52° N). In addition to the SAM locations we supplied to OCO-3 to overlap with PRISMA targets, there are many other power plant and fossil fuel combustion sources that make up its set of mission targets. However, unlike PRISMA, OCO-3 does not consider cloud forecasts, snow cover, or viewing geometry when planning SAMs and thus the majority of observations fail to produce useful maps of XCO_2. Additionally, aerosol- and albedo-induced XCO2 artifacts are present in many SAMs (Bell et al., 2023) and thus make the detection of plumes even more difficult.

For all cloud-free soundings, OCO-3 XCO2 concentrations are derived using the Atmospheric Carbon Observations from Space (ACOS; O'Dell et al., 2012; Crisp et al., 2012; O'Dell et al., 2018) v10 optimal estimation retrieval, which employs the Levenberg-Marquardt modification of the Gauss-Newton method. In this work, bias corrected XCO_2 from the OCO-3 Lite files is used but the official data quality flag is not applied. This was done because often the quality flag removes XCO_2 retrievals within the plume and makes emission estimation more difficult or impossible (Nassar et al., 2022). For SAMs where we visually identified CO_2 plumes (e.g., Figure 2), emission rates are estimated using two approaches: (1) a Gaussian plume model and (2) the IME method. For the Gaussian plume model approach, we follow the algorithm outlined in Nassar et al. (2022):

$$V(x,y) = \frac{Q}{\sqrt{2\pi}\sigma_y(x)u} e^{-(\frac{1}{2})(\frac{y}{\sigma_y(x)})^2} \quad (8)$$

$$\sigma_y(x) = a \cdot \left(\frac{x}{x_o}\right)^{0.894} \quad (9)$$

Where *V* represents the vertical columns within the plume (g/m^2), Q is the CO_2 emission rate (g/s), *y* is the wind direction perpendicular to the plume (m), *u* is the wind speed at the height of the plume at its midline (m/s) assuming plume rise of 250 m above the stack height, $\sigma_y(x)$ is the standard deviation of the *y*-direction, x_o is a characteristic plume length (1000 m), and a is a stability parameter (Nassar et al., 2021). Following Nassar et al. (2022), wind speed and direction inputs are estimated by taking the average of ERA-5 (Bell et al., 2020) and MERRA-2 reanalysis data. The wind direction is optimized by rotating the plume, typically between -30° to 30° away from the mean ERA-5/MERRA-2 direction, and calculating the correlation coefficient (*R*) of the modeled and observed XCO_2. The optimized wind direction is the direction that produces the largest *R*. The background is typically estimated by averaging OCO-3 footprints within a radius of 30 km, excluding the plume itself and a narrow 3 km buffer zone. However, if there are visible artifacts in the XCO_2 background that are unrelated to the power plant plume, the background field is modified to avoid them. For example, decreasing the radius of footprints used from 30 km to 20 km. The uncertainty in wind speed is calculated by taking the difference of the emission estimate using two different models (ERA-5 and MERRA2). The background concentration uncertainty is calculated by estimating *Q* using three different background radii of 30, 40, and 50 km. *Q* is also calculated for a 30 km radius background but only using the left and right halves of the background, relative to the direction of the plume. The standard deviation of both these methods is calculated and the larger of the two is the background uncertainty. The plume rise uncertainty is calculated by estimating Q using plume rise values of 100, 200, 250, 300, and 400 m and taking the standard deviation of those values. Total uncertainty on the emission rate *Q* using the Gaussian plume method is estimated by adding in quadrature the contribution of wind speed, background concentration, and plume rise uncertainties.

To obtain another estimate of emission rate, we also apply an IME quantification approach to the CO_2 plumes, which to our knowledge is the first time the IME method has been applied to OCO-3 SAMS at coal power plants. We first interpolate the XCO_2 retrievals in a SAM to a uniform 2×2 km^2 grid to account for occasional OCO-3 footprint overlap. Similar to Varon et al. (2018), 3×3 pixel neighborhoods are sampled and the distributions are compared to the background using a Student's *t*-test. The default confidence level for the *t* test is 95% but this is often lowered to visually capture most of the plume. The plume is then smoothed using a 3×3 pixel median filter and a Gaussian filter with a standard deviation of 0.5. The U_{eff} calculation is done using an equation approximately equal to Equation 7 ($U_{eff} = 1.0 \log U_{10} + 0.55$). Other recent studies have used various methods (Lin et al., 2023; Brunner et al., 2023), but further research is needed to determine the most accurate way to estimate U_{eff} for an OCO-3-like instrument. The wind direction is the optimized direction determined by the Gaussian plume model. The background XCO_2 estimate is taken from the Gaussian plume model methodology and the plume is typically required to be within 50 km downwind and 8 km crosswind of the source, although these parameters are modified if the plume curves outside of the 8 km crosswind threshold or there are XCO_2 artifacts that should be avoided.

The uncertainty for the IME method is estimated similarly to the Gaussian plume model method. The uncertainty in wind speed is calculated by taking the standard deviation of the emission estimates using wind speed from two different models (ERA-5 and MERRA2). The background concentration uncertainty is calculated by estimating Q using the different backgrounds calculated in the Gaussian plume model method: a 20 km radius, 30 km radius, 40 km radius, left half, full circle, and right half. The standard deviation of the three radii estimates and left half, full circle, and right half estimates are calculated and the larger of the two is the background uncertainty. Uncertainty of the Student's *t*-test confidence level is also estimated. The confidence level and -10% and +10% of the confidence level are used to find Q. For example, if the confidence level needed to visually capture the XCO_2 plume is 85%, Q is calculated for 75%, 85%, and 95% and the standard deviation of those three values represents the confidence level uncertainty. Total uncertainty on the emission rate Q using the IME method is estimated by adding in quadrature the contribution of wind speed, background concentration, and Student's *t*-test confidence level uncertainties.

Figure 2 shows IME methodology successfully identifying an XCO_2 plume from an OCO-3 SAM taken over the Colstrip power plant.

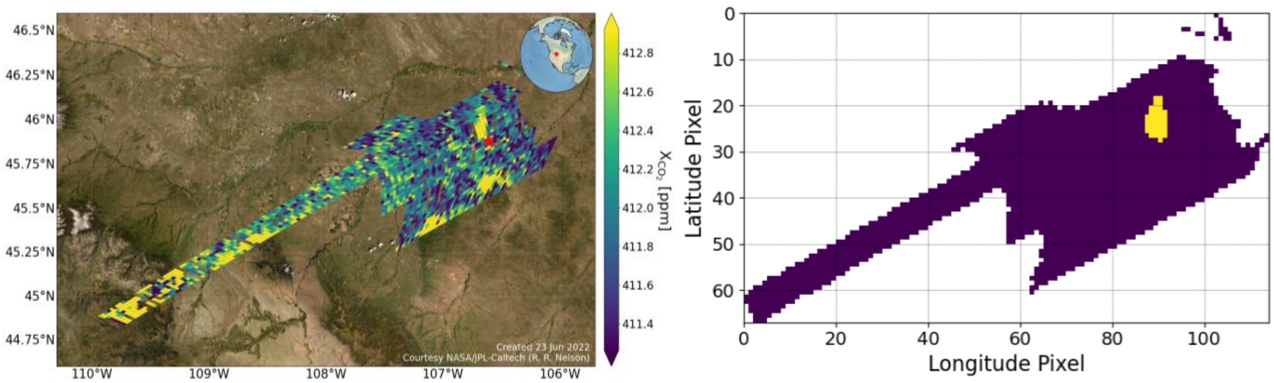

Figure 2. IME plume identification approach applied to an example OCO-3 SAM at the Colstrip power plant on 18 August 2021. Left panel: OCO-3 SAM bias corrected XCO_2. Right panel: yellow pixels indicate the final plume mask.

3 Results

3.1 Global yields from two years of observations

Figure 3a shows a global map of power plants we targeted with PRISMA, with the marker for each power plant's location (latitude, longitude) scaled to represent the number of successful acquisitions between 2021-2022. In total, we acquired 181 PRISMA images, which corresponds to

314 unique power plant observation scenes. Of these scenes, 210 were of sufficient quality to attempt CO_2 retrieval and plume detection, with quality mostly determined by visual inspection for clouds and haze. Of these 210 scenes, 104 were determined to have CO_2 plumes (Figure 3b). Scenes were marked as containing CO_2 plumes through inspection of XCO2 and visible imagery: if a large cluster of pixels with elevated XCO_2 above the background were also in the vicinity of a power plant exhaust stack, an analyst would mark the scene as containing a CO_2 plume. Routine tasking observations with PRISMA resulted in an average of 6 acquisitions for each power plant (maximum 15), roughly one image acquired per quarter. Of these acquisitions, plumes were detected on average four times per facility (maximum 12).

For OCO-3, 1363 power plant SAMs were taken during September 2019 to December 2022. Of these, 139 XCO_2 plumes emanating from power plants were visually identified. However, only 14 were for power plants that were also observed by PRISMA and have CEMS validation (nine Colstrip cases, two Martin Lake cases, and three Craig cases). The acquisition rates are low relative to PRISMA because OCO-3 does not account for scene favorability when planning its SAMs. For example, OCO-3 took 66 Colstrip SAMs from 2019-2022 yet only yielded nine high-quality XCO_2 plume cases.

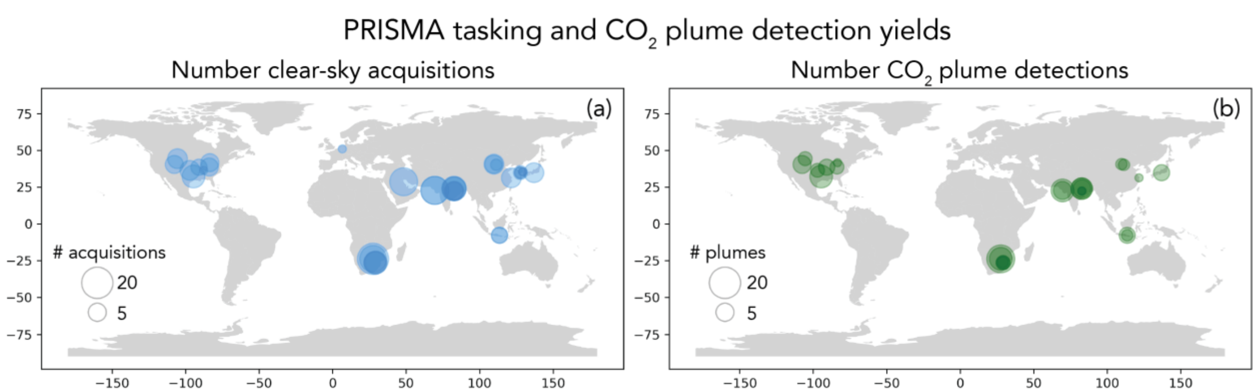

Figure 3. Data yields from PRISMA continually between 2021-2022. Panel (a) shows the number of clear-sky acquisitions for each power plant. Panel (b) shows the number of plumes detected by an analyst for each of the observed power plants.

The low observed average detection rate of CO_2 plumes is a result of three primary factors: (1) observing conditions at each facility including solar zenith angle (SZA) and surface reflectance; (2) local meteorology; and (3) operational status at each power plant at the time of acquisition. To test how well these factors predict the presence of a plume for PRISMA, we fit a logistic regression classification function with a sparse (L1) penalty to our dataset (Fan et al., 2008). This algorithm fits a logit function to the plume detection outcome of each scenes (i.e., detected plume = TRUE, no detected plume = FALSE) using a set of predictor variables that are likely candidates to explain prediction results. In this setup, the statistical model is fit using the following predictor variables – SZA, U_{10}, average single-sounding retrieval precision across the scene, annual bottom-up emission estimate for the power plant using GEM, and average observed radiance between 1900-2100 nm within the scene normalized by the cosine of the SZA. This last factor is a simple proxy for surface reflectance, although it does not take into account other factors that influence radiance observations (e.g., water vapor, aerosols, other atmospheric constituents). We split the data so that 50% was used to train the model and 50% was reserved as a test set. The predictor variables were all standardized by their mean and standard deviation before the model was fit. The results of classification can be summarized using two statistics: precision (ratio of true positives to sum of true positives and false positives) and recall (ratio of true positives to sum of true positives and false negatives). The results of fitting a logistic regression model to the data show minor prediction performance, with precision = 0.60 and recall = 0.69 for positive plume detection. The regression coefficients are shown in Figure

4a. The coefficient with the highest weight is normalized radiance. Figure 4b shows SZA against normalized radiance, with red dots indicating no plume detection and blue dots representing positive plume detection. Though no clear separation exists, there is a cluster of no plume detection at high SZA and low normalized radiance. This is a consistent and expected relationship, as SZA and surface reflectance are principal drivers of the quantity of light that is observed by the satellite, and therefore SNR of the observation.

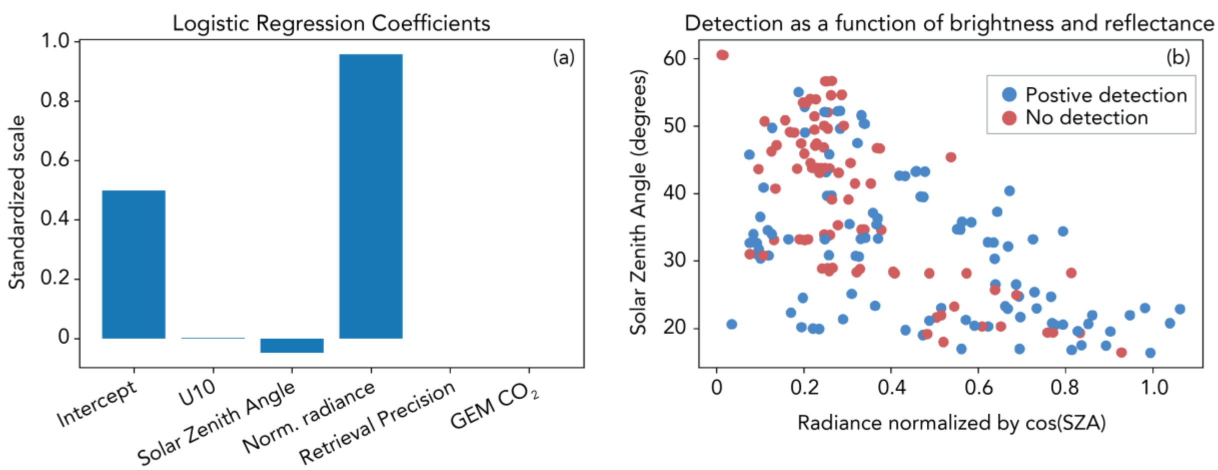

Figure 4. CO_2 plume prediction using various atmospheric, retrieval, and bottom-up information. Panel (a) shows the results of fitting a logistic regression classification model to the set of PRISMA acquisitions where an analyst identified the presence or lack of a plume. Panel (b) shows the top two explanatory variables (SZA and normalized radiance) along with plume classification.

The logistic regression model performed better on the test data set than predictions made at random, though the prediction performance was still low. Missing from the model is sub-annually resolved information regarding operating status. For most of the power plants outside the U.S., we do not have information on daily operations of a power plant. In many cases of non-detects, we could simply be observing a power plant temporarily not in operation. Another possibility is that at the time of acquisition, some power plants were operating at reduced capacity, meaning that CO_2 emission rates were lower than those predicted by annual emission factors or activity data. If the true CO_2 emission rate was below the minimum detection limit (MDL) possible by the PRISMA satellite, then it would show as a non-detect. However, even if the emission were near or slightly above the PRISMA MDL, the probability of detection would still be low as slight variations in atmospheric properties, as seen in Figure 4, would then influence the ability to detection a CO_2 plume.

3.2 Validation of PRISMA and OCO-3 emission rates against CEMS

For each power plant where a CO_2 plume was identified, we quantify emissions using the IME approach described by Equations 5-7. In order to estimate the XCO_2 mass enhancement ($\Delta\Omega$ in Equation 1), a local background must be quantified and subtracted from total XCO_2 retrievals across the scene. To do this, we apply a concentration threshold β to initiate the plume masking and segmentation process (described in Methods section). Once we have a plume mask, we apply another concentration threshold γ to the remaining XCO_2 pixels that exist outside of the plume. This value γ represents the XCO_2 background that we use to calculate the XCO_2 enhancement that is used in the IME formulation of Equation 1. Thresholds β and γ largely influence the magnitude of the emission rate and are not known a priori. For global generalizability, we wish to estimate β and γ such that they do not vary across power plants, seasons, regions, etc. Therefore, we parameterize β and γ as percentiles under the assumption that the local contrast between enhanced CO_2 plume pixels and the background should be similar across PRISMA scenes.

To estimate values for β and γ, we compare EPA CEMS data for power plants in the U.S. with estimated emission rates from PRISMA. In total, we have 12 scenes in the U.S. with CEMS information that pertain to 5 power plants. We then optimize β and γ such that the output of an ordinary least squares regression produces a slope near unity. Figure 5a shows the results of this optimization which produces an optimal β percentile of 94% and a γ percentile of 62%. The results also show decent correlation between CEMS data and PRISMA-derived emission rates ($R^2 = 0.43$). A single outlier at the Labadie power plant (imaged July 10, 2022) shows the largest discrepancy from CEMS data (69%), but the remaining plumes show average 27% relative difference from CEMS data. If we remove the one data point at Labadie, the R^2 improves to 0.75. Though a limited sample size, between PRISMA and OCO-3, these scenes represent variability in solar geometries (20-40° SZA), surface reflectance (0.09-0.90 normalized radiance), and reported emission rates (0.51 – 2.39 kt CO2 h^{-1}). Therefore, we use these optimal parameters and apply them to our global dataset of PRISMA detections. These emission rates are reported in Table 1. There are some instances when performing IME emission calculations using these thresholds and plume masking technique do not result in emission rates (e.g., the plume masking procedure produces a mask with no pixels). In these cases, we report a detection but not an emission quantification.

Figures 5b and 5c shows the comparison between OCO-3 and CEMS at some power plants that overlap with PRISMA observations (14 scenes total). OCO-3 Gaussian plume model emission rates (Fig. 5b) have an improved correlation compared to PRISMA ($R^2 = 0.51$), although with greater bias (average 47% relative difference from CEMS). The OCO-3 IME estimates (Fig. 5c) have worse R^2 (0.32) but a better RMSE (0.45 kt CO_2/hr) compared to the Gaussian plume model estimates (0.84 kt CO2/hr), with 9 of the 14 cases being within 30% of the reported CEMS emission and an average relative difference of 30% for all 14 cases. Additionally, the least squares fit for IME is closer to the 1-to-1 line than for the Gaussian plume model.

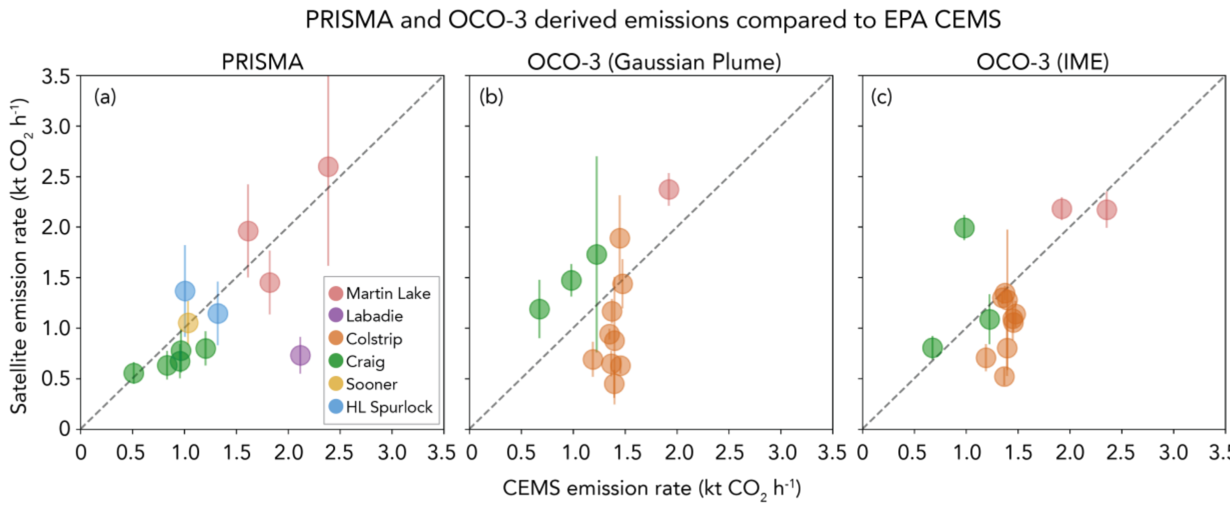

Figure 5. Comparison of emission rates in the U.S. between satellite-derived estimates and CEMS information. Panel (a) shows a comparison between PRISMA derived emission rates and CEMS (R^2 = 0.43), panel (b) shows a comparison between OCO-3 and CEMS using the Gaussian plume model (R^2 = 0.51), and panel (c) shows a comparison between OCO-3 and CEMS using IME (R^2 = 0.32).

Unique sources of error for OCO-3 emission estimates include geolocation errors in the XCO2 product. These errors are typically less than 1 km, but can be up to 2 km (Taylor et al., 2023). Errors of this magnitude, about the size of an OCO-3 footprint (~2×2 km^2), may mean that an entire footprint is not included when estimating emissions using the Gaussian plume method, which assumes that the plume only extends downwind of the known source location. The Gaussian plume model is also susceptible to wind direction errors, and requires the plume to be Gaussian in shape, which is often not true. IME, while not suffering from wind direction or geolocation-induced errors, assumes that the entire plume is captured in a given SAM, which is sometimes not true and results in an underestimation of emissions. IME is also sensitive to errors in U_{eff} parameterization.

3.3 Comparison and fusion of PRISMA and OCO

Outside the U.S., PRISMA observed the Matimba power station in South Africa 11 times and quantified emission rates 7 times. Emissions from Matimba have previously been quantified and validated using OCO-2 (Hakkarainen et al., 2021). This station does not report hourly emission rates, but does report daily power generation (Eskom, 2023). Though not a direct comparison, we can use this information to check if the emission quantification approach we describe above captures some variability in activity at this power plant. Figure 6a shows the emission rates we quantified compared against reported power generation. We see rough agreement in variability – the high power generation reported between Apr to July 2021 (70000-85000 MWh) drop for subsequent dates (47000-66000 MWh) between Sep 2021 to Sep 2022, a drop which is also seen in the PRISMA-derived CO2 emission rate. Across all observations, we estimate an emission rate range of 0.30-1.04 kt CO2 h^{-1} (average 0.66 kt CO_2 h^{-1}). This average emission rate is substantially lower than the average 2.50 kt CO_2 h^{-1} emission rate estimated from OCO-2 and TROPOMI between 2018-2020, but within the range of emissions estimates directly quantified with OCO-2 (0.30-7.20 kt CO_2 h^{-1}; Hakkarainen et al., 2021). However, this discrepancy could be result of (1) changes in activity or variability or (2) existence of other nearby emission sources. For changes in activity, during August 2020, the Matimba reported a large range of power generation (65000-94000 MWh) and emission estimates derived directly from OCO-2 were also highly variable (0.88-4.33 kt CO_2 h^{-1}). Given that maximum power generation at the time of a PRISMA observation was 85000 MWh, some of the discrepancy in maximum CO_2 quantification between PRISMA and OCO-2 could be due to activity.

Nearby (7 km) the Matimba Power Station is the Medupi Power Plant (Figure 6b). Figure 6c show the Medupi CO_2 plume observed during the same PRISMA overpass on Apr 5, 2021. The PRISMA derived emission rate for Medupi is 0.64 ± 0.26 kt CO2 h^{-1} and for Matimba is 0.73 ± 0.30

kt CO_2 h^{-1}. Given the proximity of the two power plants, the higher derived emission rate reported for Matimba from previous studies could actually be a result of a net emission from these two facilities. The OCO-2 flight track is located tens of kilometers downwind from Matimba and Medupi, making a clear delineation between potentially co-emitted distinct emission plumes near impossible. If we sum emission rates from both Medupi and Matimba, we quantify a range of 0.89-1.73 kt CO_2 h^{-1} (1.30 ± 0.28 kt CO2 h^{-1}), which is still lower, but closer to the average emissions quantified by OCO-2.

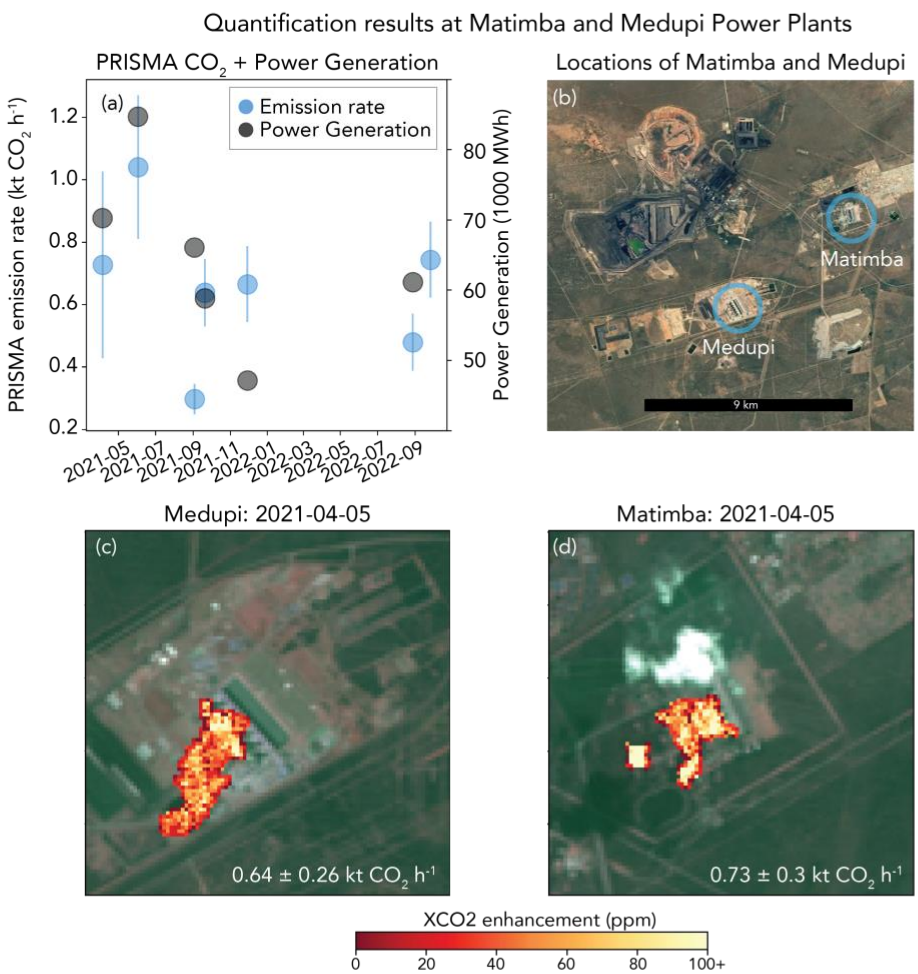

Figure 6. Emission rates and reported power generation at the Matimba and Medupi power plants in South Africa. Panel (a) shows the CO_2 emission rates derived from PRISMA and the reported daily

power generation for the day of PRISMA overpass. Panel (b) shows the locations of the Medupi and Matimba power plants (base imagery provided by Google Earth; © Google Earth 2023). Panels (c) and (d) show plume imagery and emission rates for a PRISMA overpass on Apr 5, 2021.

The ability to differentiate the contribution of unique point sources to a regional total is an application made possible by joint observing of imaging spectrometers and atmospheric sounders. Figure 7 shows observations that were made at the Tata Mundra Ultra Mega Power Plant and the Adani Mundra Thermal Power Project: two power plants less than 3 km apart. Both OCO-3 and PRISMA imaged the power plants on Apr 9, 2022. Figure 7b shows the OCO-3 SAM (taken 04:41 UTC) – large CO_2 enhancements appear along the coastline likely associated with emission from these power plants. PRISMA imaged the power plants less than two hours later (06:02 UTC) and detected CO2 plumes at each facility (Figure 7b-c). The OCO-3 derived emission rate using Gaussian plume approaches is 5.5 ± 0.7 kt CO_2 h^{-1}, but the emission rate derived using the IME approach is much lower (3.0 kt CO_2 h^{-1}). For this case, the IME approach may be more appropriate as the shape of the OCO-3 plume (Figure 7b) is more diffuse in nature and does not visibly resemble a Gaussian structure. The PRISMA emission rate for the Adani plant is 1.07 ± 0.17 kt CO_2 h^{-1} and for the Tata Mundra plant is 0.53 ± 0.08 kt CO_2 h^{-1}. We can use this information to estimate that 67% of the net CO_2 emission came from Adani, and the remaining 33% came from the Tata plant. The combined emission rate (1.60 ± 0.25 kt CO_2 h^{-1}) is lower than the OCO-3 IME emission rate. Like the Matimba power plant, some of this discrepancy may partially be explained by bias or uncertainty in retrievals, background, and wind information. Also, lower estimates of CO_2 emissions from PRISMA are consistent with the fact that PRISMA is only sensitive to emissions at two exhaust stacks, while the OCO-3 observation includes all CO_2 sources in the industrial area around Mundra. Continued validation of retrieved emission rates against ground standards (e.g., CEMS) will help better quantify bias and uncertainty. However, even with lingering uncertainty, the near simultaneous observations of OCO-3 and PRISMA can help us disentangle the relative contributions from each power plant.

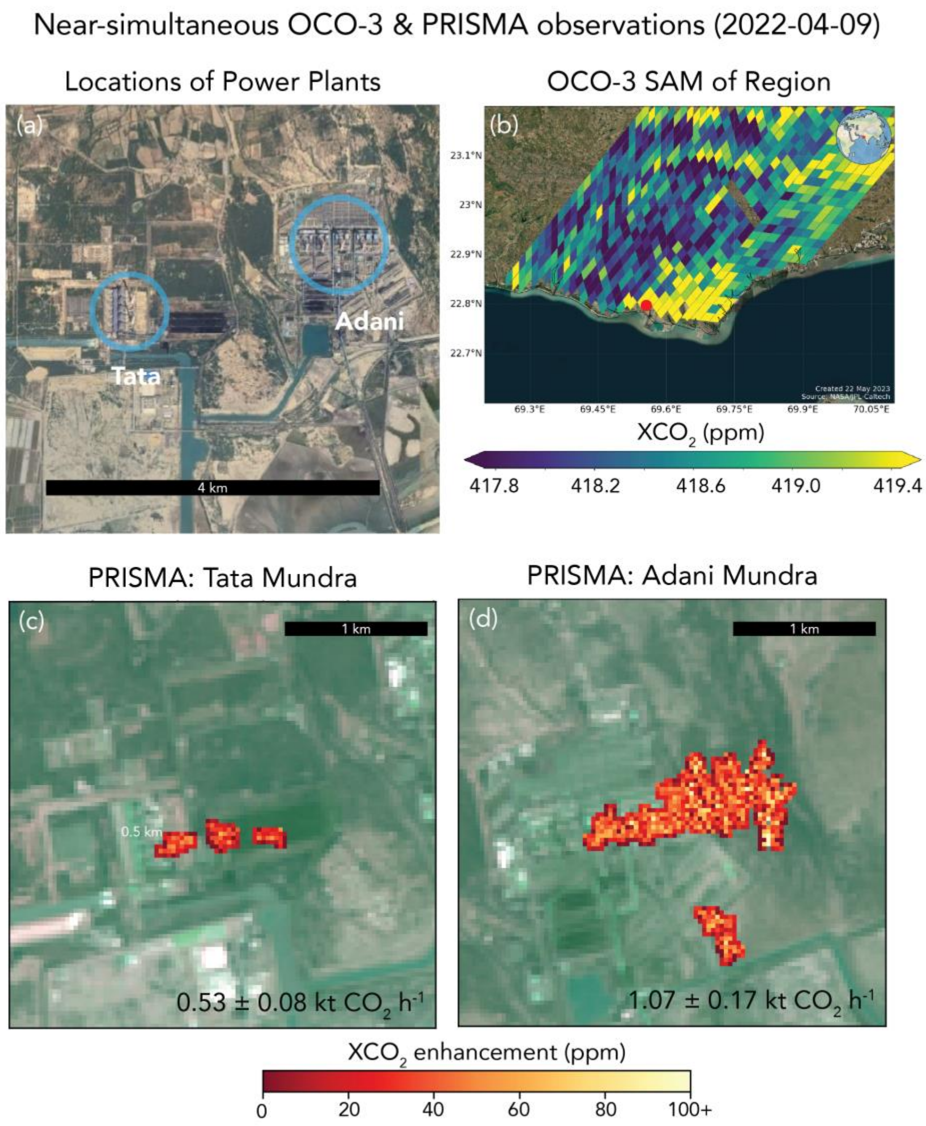

Figure 7. Near-simultaneous observation of two power plants in Mundra, India on Apr 9, 2022. Panel (a) shows the locations of two power plants spaced less than 3 km apart: Tata Mundra and Adani Mundra Power Stations (base imagery provided by Google Earth; © Google Earth 2023). Panel (b)

shows the OCO-3 SAM with a red dot showing the location of the power plants. Panel (c) and (d) show the PRISMA acquisition (less than 2 hours after OCO-3) over the two power plants with associated emission rates.

Conclusion

We observed a global set of power plants for two years between 2021-2022 with both PRISMA and OCO-3 to test the ability of these satellite platforms to do routine operational monitoring of CO_2 emissions. When PRISMA observations were of sufficient quality to perform XCO_2 retrievals, we detected CO_2 plumes nearly half of the time. We fit a logistic regression classification using plume detections and find that there is some relationship between SZA and surface reflectance that partially explains plume prediction; consistent given that these factors are major drivers of SNR. The remaining non-plume detections may be due to operational status of a power plant at the time of observation. We compared emission rates from both PRISMA and OCO-3 to power plants in the U.S. where we have access to hourly *in situ* CEMS emission information. We find significant correlation between satellite and *in situ* estimates, though some significant biases may exist for some of the observations for both PRISMA and OCO-3. Also, the quantity of CEMS observations was limited (~10 for each instrument), so robust calibration is not yet possible. Still, early results show that under the right conditions, satellites can provide reliable estimates of CO_2 emissions at discrete point source locations. This is consistent with the close agreement between airborne imaging spectrometer emissions and CEMS information (Cusworth et al., 2021).

Fusion of information from atmospheric sounders like OCO-3 and imaging spectrometers like PRISMA is valuable for cross-validation and source attribution. We see this particularly for our examples at the Matimba and Medupi power plants in South Africa and the Tata and Adani power plants in Mundra, India. In these cases, and particularly at Mundra where near-simultaneous PRISMA and OCO-3 observations were taken, OCO-2/3 provides a local, but coarse resolution emission constraint for a complex of facilities that emit large CO_2 quantities. PRISMA, with its 30 m pixel resolution, then can help refine relative contributions of single emitters against the net emission flux. More work is needed to refine cross-validation between instruments, but initial observation shows one avenue for data from multiple observing systems to be complementary aggregated and analyzed.

Even when combining information from both satellites, there is still too little sampling to constrain facility emissions within low uncertainties. Cusworth et al. (2021), using arguments from Hill and Nassar (2019), suggested that nearly 30 unbiased observations from a PRISMA-class instrument is needed per year at each power plant to reduce annual uncertainties below 14% (i.e., reduce emission uncertainty from Non-Annex I countries below 1 Gt CO_2 per year). No power plant in this study met this minimum sampling requirement. However, there will be a significant increase in data volumes and observation performance of satellite remote sensing capabilities for CO2, from both recently launched and planned imaging spectrometers including EMIT (launched 2022; Thorpe et al., in revision); EnMAP (launched 2022; Guanter et al., 2015); Carbon Mapper/Tanager 1-2 (Planned launch 2024; Duren et al., 2021), and atmospheric sounders including CO2M (Sierk et al., 2019). Improved observation of global power plants and emission quantification with robust error characterization will be vital to reduce global uncertainty of anthropogenic emissions from fossil fuel combustion sources.

Data Availability.

The OCO-3 XCO2 and other retrieval properties are publicly available at the NASA Goddard Earth Science Data and Information Services Center (GES-DISC). The full suite of retrieval products in the standard per-orbit format can be obtained at OCO Science Team et al., 2021, https://doi.org/10.5067/D9S8ZOCHCADE. The lightweight per-day format data (Lite files), which includes the bias corrected estimates of XCO2, can be obtained at OCO Science Team et al., 2022, https://doi.org/10.5067/970BCC4DHH24. PRISMA data including radiance for each scene and XCO2 retrievals is available at https://doi.org/10.5281/zenodo.8083596.

Acknowledgments. This work was supported by the Orbiting Carbon Observatory Science Team. We thank the Italian Space Agency for the PRISMA satellite targets. Portions of this work were undertaken at the Jet Propulsion Laboratory, California Institute of Technology, under contract with NASA.

Author Contributions. DHC designed the study. DHC, AKA, RJ tasked and acquired PRISMA data. DHC performed PRISMA emission quantification and validation. RRN performed OCO-3 quantification and validation. RN and JPM helped implement OCO-3 quantification algorithms. All authors provided feedback on results and the manuscript.

Competing interests. The authors declare no conflicts of interest.

References

Beirle, S., Borger, C., Dörner, S., Eskes, H., Kumar, V., de Laat, A. and Wagner, T., 2021. Catalog of NOx emissions from point sources as derived from the divergence of the NO2 flux for TROPOMI. *Earth System Science Data*, *13*(6), pp.2995-3012. DOI https://doi.org/10.5194/essd-13-2995-2021

Bell, B., Hersbach, H., Berrisford, P., Dahlgren, P., Horányi, A., Sabater, M., et al. (2020). ERA5 hourly data on pressure levels from 1950 to 1978 (preliminary version). Copernic. Clim. Change Serv. (C3S) Clim. Data Store (CDS). AvaliableAt: https://cds.climate.copernicus-climate.eu/cdsapp#!/dataset/reanalysis-era5-pressure-levels-preliminary-back-extension?tab=overview.

Bell, E., O'Dell, C.W., Taylor, T.E., Merrelli, A., Nelson, R.R., Kiel, M., Eldering, A., Rosenberg, R. and Fisher, B., 2023. Exploring bias in the OCO-3 snapshot area mapping mode via geometry, surface, and aerosol effects. *Atmospheric Measurement Techniques*, *16*(1), pp.109-133. DOI https://doi.org/10.5194/amt-16-109-2023

Brunner, D., Kuhlmann, G., Henne, S., Koene, E., Kern, B., Wolff, S., Voigt, C., Jöckel, P., Kiemle, C., Roiger, A. and Fiehn, A., 2023. Evaluation of simulated CO2 power plant plumes from six high-resolution atmospheric transport models. *Atmospheric Chemistry and Physics*, *23*(4), pp.2699-2728. DOI https://doi.org/10.5194/acp-23-2699-2023

Crippa, M., Guizzardi, D., Banja, M., Solazzo, E., Muntean, M., Schaaf, E., Pagani, F., Monforti-Ferrario, F., Olivier, J., Quadrelli, R., Risquez Martin, A., Taghavi-Moharamli, P., Grassi, G., Rossi, S., Jacome Felix Oom, D., Branco, A., San-Miguel-Ayanz, J. and Vignati, E., CO2 emissions of all world countries - 2022 Report, EUR 31182 EN, Publications Office of the European Union, Luxembourg, 2022, doi:10.2760/730164, JRC130363

Crisp, D., Fisher, B.M., O'Dell, C., Frankenberg, C., Basilio, R., Bösch, H., Brown, L.R., Castano, R., Connor, B., Deutscher, N.M. and Eldering, A., 2012. The ACOS CO2 retrieval algorithm–part II: global XCO2 data characterization. *Atmospheric Measurement Techniques*, *5*(4), pp.687-707. DOI https://doi.org/10.5194/amt-5-687-2012

Cusworth, D.H., Duren, R.M., Thorpe, A.K., Eastwood, M.L., Green, R.O., Dennison, P.E., Frankenberg, C., Heckler, J.W., Asner, G.P. and Miller, C.E., 2021. Quantifying global power plant carbon dioxide emissions with imaging spectroscopy. *AGU Advances*, *2*(2), p.e2020AV000350. DOI https://doi.org/10.1029/2020AV000350

Dougherty, E.R., 1992. An introduction to morphological image processing. In *SPIE*. Optical Engineering Press.

Duren, R., Cusworth, D., Ayasse, A., Herner, J., Thorpe, A., Falk, M., Heckler, J., Guido, J., Giuliano, P., Chapman, J. and Green, R., 2021, December. Carbon Mapper: on-orbit performance predictions and airborne prototyping. In *AGU Fall Meeting Abstracts* (Vol. 2021, pp. A53F-05).

Eldering, A., Taylor, T.E., O'Dell, C.W. and Pavlick, R., 2019. The OCO-3 mission: measurement objectives and expected performance based on 1 year of simulated data. *Atmospheric Measurement Techniques*, *12*(4), pp.2341-2370. DOI https://doi.org/10.5194/amt-12-2341-2019

Fan, R.E., Chang, K.W., Hsieh, C.J., Wang, X.R. and Lin, C.J., 2008. LIBLINEAR: A library for large linear classification. *the Journal of machine Learning research*, *9*, pp.1871-1874. DOI https://doi.org/10.5555/1390681.1442794

Gelaro, R., McCarty, W., Suárez, M.J., Todling, R., Molod, A., Takacs, L., Randles, C.A., Darmenov, A., Bosilovich, M.G., Reichle, R. and Wargan, K., 2017. The modern-era retrospective analysis for research and applications, version 2 (MERRA-2). *Journal of climate*, *30*(14), pp.5419-5454. https://doi.org/10.1175/JCLI-D-16-0758.1

GEM, Global Energy Monitor's Global Coal Plant Tracker, URL https://globalenergymonitor.org/projects/global-coal-plant-tracker/tracker/, last accessed May 24, 2023

Guan, D., Liu, Z., Geng, Y., Lindner, S. and Hubacek, K., 2012. The gigatonne gap in China's carbon dioxide inventories. *Nature Climate Change*, *2*(9), pp.672-675. DOI https://doi.org/10.1038/nclimate1560

Guanter, L., Kaufmann, H., Segl, K., Foerster, S., Rogass, C., Chabrillat, S., Kuester, T., Hollstein, A., Rossner, G., Chlebek, C. and Straif, C., 2015. The EnMAP spaceborne imaging spectroscopy mission for earth observation. *Remote Sensing*, *7*(7), pp.8830-8857. DOI https://doi.org/10.3390/rs70708830

Guo, W., Shi, Y., Liu, Y. and Su, M., 2023. CO2 emissions retrieval from coal-fired power plants based on OCO-2/3 satellite observations and a Gaussian plume model. *Journal of Cleaner Production*, *397*, p.136525. DOI https://doi.org/10.1016/j.jclepro.2023.136525

Hakkarainen, J., Szeląg, M.E., Ialongo, I., Retscher, C., Oda, T. and Crisp, D., 2021. Analyzing nitrogen oxides to carbon dioxide emission ratios from space: A case study of Matimba Power Station in South Africa. *Atmospheric Environment: X*, *10*, p.100110. DOI https://doi.org/10.1016/j.aeaoa.2021.100110

Hill, T. and Nassar, R., 2019. Pixel size and revisit rate requirements for monitoring power plant CO2 emissions from space. *Remote Sensing*, *11*(13), p.1608. DOI https://doi.org/10.3390/rs11131608

Hong, C., Zhang, Q., He, K., Guan, D., Li, M., Liu, F. and Zheng, B., 2017. Variations of China's emission estimates: response to uncertainties in energy statistics. *Atmospheric Chemistry and Physics*, *17*(2), pp.1227-1239. DOI https://doi.org/10.5194/acp-17-1227-2017

IPCC, 2021: *Climate Change 2021: The Physical Science Basis. Contribution of Working Group I to the Sixth Assessment Report of the Intergovernmental Panel on Climate Change*[Masson-Delmotte, V., P. Zhai, A. Pirani, S.L. Connors, C. Péan, S. Berger, N. Caud, Y. Chen, L. Goldfarb, M.I. Gomis, M. Huang, K. Leitzell, E. Lonnoy, J.B.R. Matthews, T.K. Maycock, T. Waterfield, O. Yelekçi, R. Yu, and B. Zhou (eds.)]. Cambridge University Press, Cambridge, United Kingdom and New York, NY, USA, In press, doi:10.1017/9781009157896.

J. Muñoz-Sabater, Dutra, E., Agustí-Panareda, A., Albergel, C., Arduini, G., Balsamo, G., Boussetta, S., Choulga, M., Harrigan, S., Hersbach, H., Martens, B., Miralles, D. G., Piles, M., Rodríguez-Fernández, N. J., Zsoter, E., Buontempo, C., and Thépaut, J.-N.: ERA5-Land: A state-of-the-art global reanalysis dataset for land applications, Earth Syst. Sci. Data,13, 4349–4383, 2021. https://doi.org/10.5194/essd-13-4349-2021.

Kochanov, R.V., Gordon, I.E., Rothman, L.S., Wcisło, P., Hill, C. and Wilzewski, J.S., 2016. HITRAN Application Programming Interface (HAPI): A comprehensive approach to working with spectroscopic data. *Journal of Quantitative Spectroscopy and Radiative Transfer*, *177*, pp.15-30. DOI https://doi.org/10.1016/j.jqsrt.2016.03.005

Lin, X., van der A, R., de Laat, J., Eskes, H., Chevallier, F., Ciais, P., Deng, Z., Geng, Y., Song, X., Ni, X. and Huo, D., 2023. Monitoring and quantifying CO2 emissions of isolated power plants from space. *EGUsphere*, pp.1-20. DOI https://doi.org/10.5194/egusphere-2022-1490

Loizzo, R., Guarini, R., Longo, F., Scopa, T., Formaro, R., Facchinetti, C. and Varacalli, G., 2018, July. PRISMA: The Italian hyperspectral mission. In *IGARSS 2018-2018 IEEE International Geoscience and Remote Sensing Symposium* (pp. 175-178). IEEE. DOI https://doi.org/ 10.1109/IGARSS.2018.8518512

Nassar, R., Hill, T.G., McLinden, C.A., Wunch, D., Jones, D.B. and Crisp, D., 2017. Quantifying CO2 emissions from individual power plants from space. *Geophysical Research Letters*, *44*(19), pp.10-045. DOI https://doi.org/10.1002/2017GL074702

Nassar, R., Mastrogiacomo, J.P., Bateman-Hemphill, W., McCracken, C., MacDonald, C.G., Hill, T., O'Dell, C.W., Kiel, M. and Crisp, D., 2021. Advances in quantifying power plant CO2 emissions with OCO-2. *Remote Sensing of Environment*, *264*, p.112579. DOI https://doi.org/10.1016/j.rse.2021.112579

Nassar, R., Moeini, O., Mastrogiacomo, J.P., O’Dell, C.W., Nelson, R.R., Kiel, M., Chatterjee, A., Eldering, A. and Crisp, D., 2022. Tracking CO2 emission reductions from space: A case study at Europe’s largest fossil fuel power plant. *Frontiers in Remote Sensing*, *3*, p.98. DOI https://doi.org/10.3389/frsen.2022.1028240

O'Dell, C.W., Connor, B., Bösch, H., O'Brien, D., Frankenberg, C., Castano, R., Christi, M., Eldering, D., Fisher, B., Gunson, M. and McDuffie, J., 2012. The ACOS CO 2 retrieval algorithm–Part 1: Description and validation against synthetic observations. *Atmospheric Measurement Techniques*, *5*(1), pp.99-121. DOI https://doi.org/10.5194/amt-5-99-2012

O'Dell, C.W., Eldering, A., Wennberg, P.O., Crisp, D., Gunson, M.R., Fisher, B., Frankenberg, C., Kiel, M., Lindqvist, H., Mandrake, L. and Merrelli, A., 2018. Improved retrievals of carbon dioxide from Orbiting Carbon Observatory-2 with the version 8 ACOS algorithm. *Atmospheric Measurement Techniques*, *11*(12), pp.6539-6576. DOI https://doi.org/10.5194/amt-11-6539-2018

Rodgers, C.D., 2000. *Inverse methods for atmospheric sounding: theory and practice* (Vol. 2). World scientific.

Reuter, M., Buchwitz, M., Schneising, O., Krautwurst, S., O'Dell, C.W., Richter, A., Bovensmann, H. and Burrows, J.P., 2019. Towards monitoring localized CO2 emissions from space: co-located regional CO2 and NO2 enhancements observed by the OCO-2 and S5P satellites. *Atmospheric Chemistry and Physics*, *19*(14), pp.9371-9383. DOI https://doi.org/10.5194/acp-19-9371-2019

Sierk, B., Bézy, J.L., Löscher, A. and Meijer, Y., 2019, July. The European CO2 Monitoring Mission: observing anthropogenic greenhouse gas emissions from space. In *International Conference on Space Optics—ICSO 2018* (Vol. 11180, pp. 237-250). SPIE. DOI https://doi.org/ 10.1117/12.2535941

Taylor, T.E., O'Dell, C.W., Baker, D., Bruegge, C., Chang, A., Chapsky, L., Chatterjee, A., Cheng, C., Chevallier, F., Crisp, D. and Dang, L., 2023. Evaluating the consistency between OCO-2 and OCO-3 XCO 2 estimates derived from the NASA ACOS version 10 retrieval algorithm. *Atmospheric Measurement Techniques Discussions*, *2023*, pp.1-61. DOI https://doi.org/10.5194/amt-16-3173-2023

Thorpe, A.K., Frankenberg, C., Thompson, D.R., Duren, R.M., Aubrey, A.D., Bue, B.D., Green, R.O., Gerilowski, K., Krings, T., Borchardt, J. and Kort, E.A., 2017. Airborne DOAS retrievals of methane, carbon dioxide, and water vapor concentrations at high spatial resolution: application to

AVIRIS-NG. *Atmospheric Measurement Techniques*, *10*(10), pp.3833-3850. DOI https://doi.org/10.5194/amt-10-3833-2017

Van Geffen, J., Boersma, K.F., Eskes, H., Sneep, M., Ter Linden, M., Zara, M. and Veefkind, J.P., 2020. S5P TROPOMI NO2 slant column retrieval: Method, stability, uncertainties and comparisons with OMI. *Atmospheric Measurement Techniques*, *13*(3), pp.1315-1335. DOI https://doi.org/10.5194/amt-13-1315-2020

Varon, D.J., Jacob, D.J., McKeever, J., Jervis, D., Durak, B.O., Xia, Y. and Huang, Y., 2018. Quantifying methane point sources from fine-scale satellite observations of atmospheric methane plumes. *Atmospheric Measurement Techniques*, *11*(10), pp.5673-5686. DOI https://doi.org/10.5194/amt-11-5673-2018